Soft Matter

Multiplexed and Continuous Microfluidic Sensors using Dynamic Complex Droplets

Journal:	*Soft Matter*
Manuscript ID	SM-ART-01-2023-000074.R1
Article Type:	Paper
Date Submitted by the Author:	10-Feb-2023
Complete List of Authors:	Barua, Baishali; The University of Arizona, Chemical and Environmental Engineering Durkin, Tyler; The University of Arizona, Chemical and Environmental Engineering Beeley, Isabel; The University of Arizona, Chemical and Environmental Engineering Gadh, Aakanksha; The University of Arizona, Chemical and Environmental Engineering Savagatrup, Suchol; The University of Arizona, Chemical and Environmental Engineering

Multiplexed and Continuous Microfluidic Sensors using Dynamic Complex Droplets

Baishali Barua, Tyler J. Durkin, Isabel M. Beeley, Aakanksha Gadh, and Suchol Savagatrup*

Department of Chemical and Environmental Engineering, University of Arizona, 1133 E. James E. Rogers Way, Tucson Arizona 85721

* Authors to whom correspondence should be addressed: S.S. (suchol@arizona.edu)

Keywords: complex emulsions, interfacial tensions, PDMS microfluidics, multiplexed, real-time, sensors

ABSTRACT: Emissive complex droplets with reconfigurable morphology and dynamic optical properties offer exciting opportunities as chemical sensors due to their stimuli-responsive characteristics. In this work, we demonstrated a real-time optical sensing platform that combines poly(dimethylsiloxane) (PDMS) microfluidics and complex droplets as sensing materials. We utilized a mechanism, called *directional emission*, to transduce changes in interfacial tension into optical signals. We discuss the fabrication and integration of PDMS microfluidics with complex emulsions to facilitate continuous measurement of fluorescent emission and, ultimately, the interfacial tensions. Furthermore, by varying the interfacial functionalization and fluorescent dye with characteristic wavelength, we generate multiple formulations of droplets and obtain differential responses to stimuli that alter interfacial tensions (*i.e.*, composition of surfactants, pH). Our results illustrate a proof-of-concept multiplexed and continuous sensing platform with potential applications in miniaturized, on-site environmental monitoring, and biosensing.

INTRODUCTION

Complex emulsions are an important class of materials for applications in pharmaceutical formulations, medical diagnostics, drug delivery, and chemical sensing.[1–4] In the context of sensing applications, these all-liquid materials are extremely sensitive to changes in interfacial tensions and are able to dynamically and reversibly transform their physical morphology and optical properties in the presence of chemical analytes.[5–11] For example, they have previously been demonstrated as effective detection platforms for biological analytes—such as *E. coli*,[12,13] *Listeria monocytogenes*,[14,15] SARS-CoV-2,[16,17] and bacteriophages[18]—as well as environmental contaminants.[19,20] While these examples served as successful proofs-of-concept, crucial limitations exist that prevent the development of an on-site sensing platform for real-world samples and situations. Specifically, many of the current platforms lack the capacity to generate multiplexed or continuous sensing signals.[21,22] Moreover, methods to integrate these capabilities with complex emulsions towards more practical sensing devices have not been emphasized.

In fact, selective and timely identification of complex chemical mixtures is essential in environmental monitoring and clinical diagnostics.[23–27] The "need for speed" often stands in direct contrast to most classical analytical and bioanalytical strategies, which necessitate prolonged processes and specialized instruments.[28,29] Moreover, transportation of the samples to a well-equipped laboratory could further extend the time needed for identification.[30,31] To mitigate these concerns, a rapid analytical tool should allow users to investigate a sample for many targeted analytes (*i.e.*, multiplexed, high-throughput screening) and enable prescreening or semi-quantitative diagnostics.[32,33] Furthermore, continuous detection of chemical analytes is essential for real-time monitoring of environmental health. Such information could be used, for example, to understand the fate of emerging contaminants, model transport phenomena, and formulate plans of treatment with a closed-loop feedback control.[34–37] However, the integration of platforms with multiplexed detection and continuous

monitoring remains limited to large-scale operations, rather than smaller-scale, rapid, and on-site applications.[23,25,27]

As an alternative, complex emulsions provide a promising framework for on-site, multiplexed, and continuous sensing devices. Previous works by our group and others have used the coupling between the dynamic morphology and optical properties of complex emulsions for the selective detection of targeted analytes.[11,12,15,17–20,38,39] For example, Zeininger et al. reported detections of *Salmonella enterica* using the relationship between the internal geometry of the droplets (induced by the presence of the bacteria) and the angular distribution of fluorescent emission.[11] This transduction mechanism, called *directional emission*, has also been used to detect trace concentrations of per- and polyfluoroalkyl substances (PFAS)[20] and hydrogen peroxide.[39] In these examples, changes in interfacial tensions at the interfaces of complex droplets altered the physical morphology of the droplets and produced optical signals. Thus, this mechanism is, at its core, a measurement of interfacial tensions. However, unlike classical techniques such as force or pendant drop tensiometry, it can be engineered to probe multiple interfaces simultaneously. Specifically, the interface of each droplet can be functionalized to behave as an independent probe within the same system.[11,15,17,40] Thus, we hypothesized that each functionalized droplet and its interface will produce differential measurements of interfacial tensions. That is, the use of complex droplets may allow for the monitoring of multiple analytes within the same complex system.

Furthermore, we sought to combine the dynamic properties of these complex droplets with microfluidic devices to produce real-time measurements. Microfluidics have been used in sensing applications to enable rapid, real-time, and in-line measurement of molecular interactions. These sensors combine microscale sensing operations—such as electrochemical and optical sensors—with a controllable flow of analytes to produce "lab-on-a-chip" devices.[41–45] The measurement of interfacial tensions using microfluidic devices (microtensiometry) was pioneered by Hudson and co-workers[46,47] and has been extensively studied by many researchers.[48–55] These methods rely on the manipulation of microfluidic flows and the deformation of immiscible liquid droplets to quantitatively measure interfacial tensions. While successful, these studies rely on an accurate flow field and the visualization of complex deformation geometry of single droplets, which could potentially hinder the ability to produce high-throughput results and multiplexing capability.

Herein, we present a coupling of complex droplets and microfluidic devices to produce a sensing platform with the capability to measure multiple interfaces simultaneously and continuously. Specifically, we demonstrated that emissive complex droplets with different interfacial functionalization embedded into poly(dimethylsiloxane) (PDMS) microfluidic devices can generate measurements that are both independent and continuous. We then leveraged the sensing mechanism of emissive complex droplets (*i.e.*, directional emission) to transduce real-time changes in the concentrations of hydrocarbon and fluorocarbon surfactants and the effectiveness of polymeric surfactants into optical signals (*i.e.*, changes in emission intensity). This combination of emissive complex droplets and a PDMS microfluidic setup provides a proof-of-concept of in-line measurement for applications in environmental monitoring. The core innovation of our approach is the ability to optically measure interfacial tensions through complex droplets with the in-line, real-time, continuous measurement afforded by microfluidic platforms.

EXPERIMENTAL DESIGN

Choice of emissive complex droplets. Each all-liquid droplet comprised an equal volume of hydrocarbon oil (H-oil) and fluorocarbon oil (F-oil) with a fluorescent dye dissolved in the H-oil (**Figure 1**). Several design parameters were chosen to optimally transduce changes in interfacial tensions to optical signals (*i.e.*, changes in emission intensity). First, the complex droplets must be gravity-aligned with H-oil oriented on top of F-oil. Thus, we selected toluene as the H-oil and a 9:1 mixture of 3-ethoxyperfluoro(2-methylhexane) (HFE-7500) and perfluorotributylamine (FC-43) as the F-oil due to the difference in densities. Specifically, the density of toluene (0.867 g cm^{-3}) is significantly lower than those of the F-oils (1.614 g cm^{-3} for HFE-7500 and 1.86 g cm^{-3} for FC-43). FC-43 was added to HFE-7500 to adjust the temperature in which the F-oil mixture would become miscible with toluene (H-oil).[11] Secondly, the overall density of the complex droplets must be higher than water to ensure that the droplets remain fully submerged. For this reason, we selected ortho-dichlorobenzene (ODCB) (1.3 g cm^{-3}) for control experiments with single-phase droplets. Thirdly, this optical transduction mechanism relies on total internal reflection at the H-oil/F-oil interface.[11,20,39,56] Therefore, the refractive index of the H-oil (n = 1.49) must be significantly higher than that

of the F-oil mixture (n = 1.29).[11] Lastly, we chose three fluorescent dyes with distinctive characteristic emission wavelengths: perylene (λ_1~ 475 nm), coumarin 545T (λ_2~ 505 nm), and lumogen red F300 (λ_3~ 610 nm) (**Supporting Information, Figure S1**).

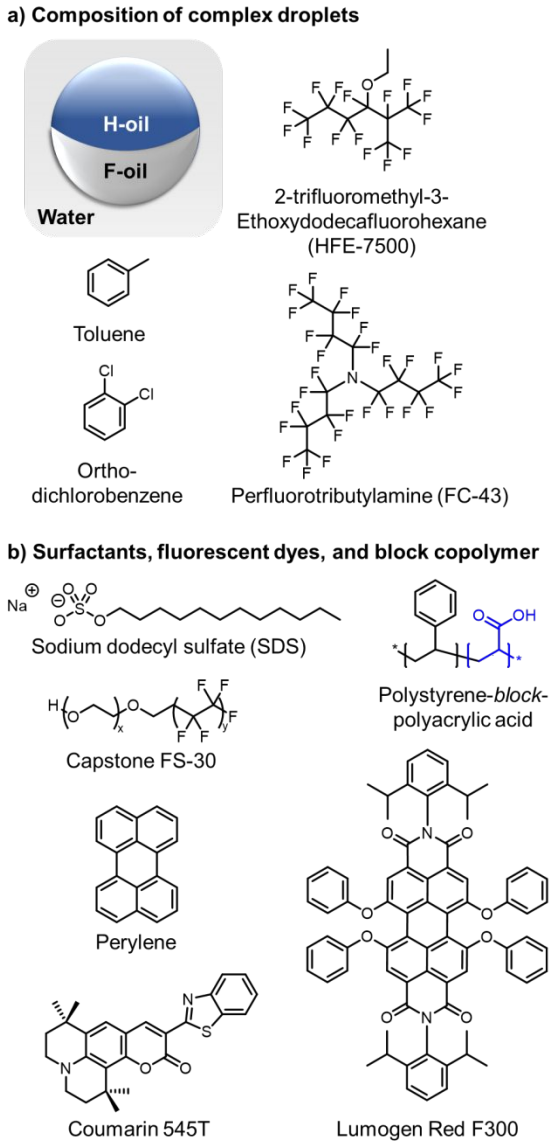

Figure 1. (a) Side-view schematic of a complex droplet and chemical structures of hydrocarbon oils (H-oil) and fluorocarbon oils (F-oil). (b) Chemical structures of surfactants and the fluorescent dyes used in this study.

To both stabilize the complex droplets and modulate their dynamic transformation, we chose sodium dodecyl sulfate (SDS) and Capstone FS-30 as the hydrocarbon surfactant (H-surfactant) and fluorocarbon surfactant (F-surfactant), respectively. Both surfactants are commonly used with dynamic complex droplets.[5,20,57] In certain formulations of our system, we used an amphiphilic block copolymer, polystyrene-*block*-polyacrylic acid (PS-*b*-PAA), to create pH responsive complex droplets. Polyacrylic acid, the hydrophilic segment of the block copolymer, is known to be sensitive to pH changes and undergoes a reversible conformational transformation from an extended coil (at high pH) to a compacted globule (at low and neutral pH).[58] This transformation alters the interfacial tensions and creates a driving force to transform the morphologies of complex droplets.[59,60]

Fabrication of emissive complex droplets. Optical properties (*i.e.*, fluorescent emission intensity) of complex droplets depend on their internal geometry and overall size.[11,20] We used monodispersed droplets to isolate the two sources and to focus exclusively on the effects from internal geometry. Each formulation of droplets was fabricated and characterized prior to its incorporation into microfluidic-based sensors. We followed previously reported methods to generate droplets with highly uniform composition and size.[5,11,57] Briefly, equal volumes of H-oil containing dissolved fluorescent dye and F-oil were heated above their upper critical temperature (T_c) to produce a single miscible dispersed phase. This solution was then emulsified in an aqueous solution of SDS using a Dolomite Microfluidic Setup within an incubator that maintained temperature above T_c. We used two Mitos pressure pumps to control the flow rates of the continuous phase (SDS solution) and the dispersed phase (miscible mixture of H-oil with fluorescent dye and F-oil) through a flow-focusing chip with a channel size of 50 µm. After cooling to room temperature, each batch was characterized via optical and fluorescent microscopy. This fabrication method produced monodispersed droplets (diameter: 49 ± 3.6 µm) with distinct H-oil and F-oil domains (**Supporting Information**, **Figure S2**). All sensing experiments were performed using monodispersed droplets to create an easily reproducible monolayer and to eliminate the size effects on optical emission read-out.

Design and fabrication of PDMS microfluidic-based sensors. We selected PDMS microfluidic devices because they provide a facile method to generate prototypes and their fabrication procedures have been well documented in literature.[61–64] Furthermore, PDMS is transparent in the visible range, which is essential in order to observe the fluorescent emission of embedded complex droplets. The microchannels were constructed via soft lithography by casting uncured PDMS (10:1 base:crosslinker mixture) onto a reverse mold of patterned SU-8 photoresist on a silicon wafer. After complete curing at room temperature, inlet and outlet holes were added using disposable biopsy punches, and

the patterned layer was plasma bonded to an additional layer of flat PDMS and a glass slide for support. The microfluidic setup used in our sensing experiment comprised three separate sections: (1) a mixing channel, (2) a bubble trap, and (3) a droplet sensing chamber (**Supporting Information, Figures S3**). The serpentine-shaped mixing channel was included to fully mix the inlet streams from multiple syringe pumps. The bubble trap was added downstream of the mixing channel to remove any bubbles introduced by the syringe pumps or generated during the mixing process. The presence of bubbles may interfere with the optical reading and mechanically agitate the droplets. Finally, the sensing chamber was placed downstream of the bubble trap to hold complex droplets stationary in a monolayer. Because complex droplets are denser than water, they self-assemble into a hexagonal close-packed monolayer at the bottom of the sensing chamber. We then placed a bifurcated optical fiber directly above the chamber to both excite the fluorescent dye with a UV light (λ = 405 nm) and to collect the emission spectra as a function of time through a connected spectrophotometer (**Figure 2a**).

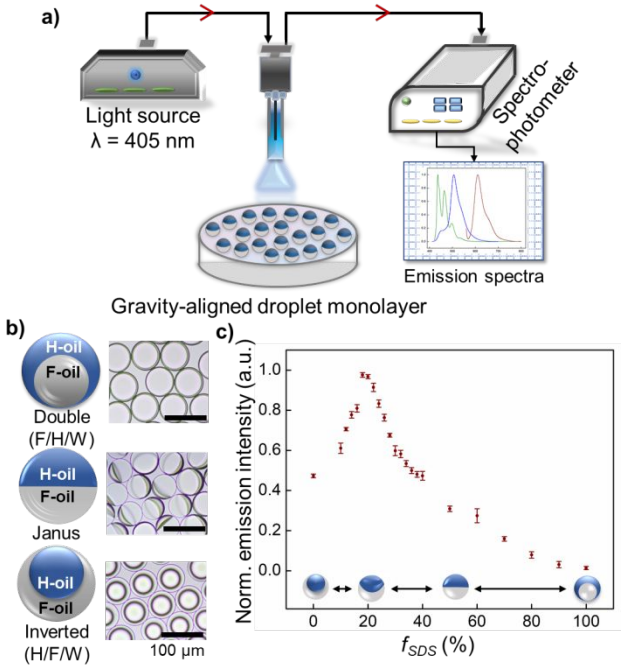

Figure 2. (a) Schematic diagram of the sensing setup, comprising a sensing chamber with a monolayer of complex droplets and a bifurcated optical fiber that transmits UV light (λ = 405 nm) and collects real-time emission spectra via a spectrophotometer. (b) Side-view schematic diagrams and top-view optical micrographs of the different morphologies of complex droplets: double emulsion (F-oil in H-oil in water, F/H/W), Janus (two hemispheres of H-oil and F-oil), and inverted emulsion (H-oil in F-oil in water, H/F/W). (c) Normalized emission intensity as a function of the overall fraction of hydrocarbon surfactant (SDS) with fluorocarbon surfactant (Capstone) as the other fraction. The error bars represent the standard deviations of repeated measurements ($N \geq 6$).

Sensing mechanisms of complex droplet-based microfluidic sensors. We leveraged a mechanism, called directional emission, that relates the fluorescent emission of complex droplets to changes in interfacial tensions.[11,20,39,56] Specifically, the morphology of complex emulsions depends on the balance of interfacial tensions between the H-oil/water interface (γ_H) and F-oil/water interface (γ_F), (**Figure 2b**).[15] For example, in an aqueous solution with a higher concentration of H-surfactants, the value of γ_H is smaller than γ_F. Thus, the H-oil/water interface is favored over the F-oil/water interface, leading to a droplet morphology in which H-oil encapsulates F-oil in a double emulsion (F/H/W). In the opposite scenario where γ_F is smaller than γ_H, F-oil encapsulates H-oil in an inverted emulsion (H/F/W). The transformation between these two end points is dynamic and reversible. That is, when the values of γ_H and γ_F are similar, the droplets assume a Janus morphology. Importantly, this change in morphology significantly affects the direction and intensity of the scattered emissive fluorescent light. Because of the difference between the refractive indices of H-oil and F-oil, the interface between the two facilitates total internal reflection (TIR)within each droplet. Thus, the intensity of the fluorescent emission collected vertically above the droplets varies depending on the morphology, and ultimately on γ_H and γ_F. **Figure 2c** demonstrates the relationship between the normalized emission and the fraction of the H-surfactant (SDS), f_{SDS}. The value f_{SDS} is commonly used as a proxy for the ratio between γ_H and γ_F,[5,11,20,39,56] and is defined as the ratio of the concentration of SDS to the combined concentration of SDS and Capstone: $f_{SDS} = \frac{[SDS]}{[SDS]+[Capstone]}$. Our observed relationship agrees with previous reports that showed similar behavior and maximum intensity occurring near f_{SDS} of 0.20.[11,20,39,56] This value of f_{SDS} leads to the morphology with the triple-phase contact angle that directs the majority of TIR light vertically toward the detector. Furthermore, we observed that the identity of the dye does not affect the general behavior of directional emission; additional experiments with coumarin 545T (measured at λ = 505 nm) and lumogen red F300 (measured at λ = 610 nm) are shown in **Supporting Information, Figure S4**. We note here normalized values of the measured emission intensities were used to provide internal references and to effectively compare between experiments (**Supporting Information S5**). Briefly, we measured the maximum and minimum values for each

formulation of droplets and normalized other measurements into a range between 0 and 1.

RESULTS AND DISCUSSIONS

Combination of PDMS microfluidic chips and emissive complex droplets. **Figures 3a–b** show a schematic diagram and photograph of our sensing setup, including two syringe pumps, PDMS microfluidic modules, and a bifurcated optical fiber connected to a UV light source and a spectrophotometer. As a proof-of-concept, we used two programmable syringe pumps to inject analyte solutions through the microchannels at different flow rates, durations, and flow ratios. The two syringe pumps were filled with pure solutions of SDS and Capstone. Thus, by controlling the ratio between the two flow rates, we can adjust the concentrations of the surfactants and ultimately the interfacial tensions γ_H and γ_F. The use of syringe pump simulates an in-line operation for the detection of contaminants in water, in which a small stream of sample solution would be diverted from the mainline into a continuous sensing platform.[65]

We fabricated the three-stage PDMS microfluidic modules consisting of (1) a mixing channel, (2) a bubble trap, and (3) a sensing chamber, all connected via PTFE tubes (*inner diameter = 0.5 mm*). The mixing channel was designed with serpentine microchannels to facilitate passive mixing of laminar flows.[66,67] We confirmed that two inlet streams of surfactant solutions were sufficiently mixed at the outlet of the mixing channel at the experimental flow rates (**Supporting Information, Figure S5**). This mixed outlet stream next enters a vertical cylindrical-shaped microcavity (*volume* = 20 μL), which traps air bubbles by providing additional dead volume.[68] Removing bubbles is critical because they may interfere with measured fluorescence intensity or mechanically agitate the complex droplets.[11,57] The third module is the sensing chamber (*diameter* = 5 mm, *depth* = 3 mm), which holds a monolayer of droplets and is connected to the inlet and outlet streams via a thin rectangular microchannel (*width* = 0.5 mm, *depth* = 110 μm), (**Figures 3c–e**). Prior to each experiment, every PDMS module was flushed with 0.1 M NaOH solution and then rinsed with Milli-Q water to ensure that the inner surfaces were sufficiently hydrophilic.[69] We then pipetted a surfactant solution containing emissive complex droplets into the chamber to generate a monolayer array (**Figure 3f**). We maintained a constant total volume (20 μL) of droplets withdrawn from the bulk to create a reproducible monolayer inside the sensing chamber for every experiment. This monolayer of monodispersed droplets is critical to the reproducibility of the measured emission intensities.[11] We note here that while PDMS is not known to swell when in direct contact with water or fluorocarbon oils, hydrocarbon oils are known to swell PDMS.[70,71] Thus, we circumvented this potential issue by (i) sufficiently stabilizing complex droplets with surfactant solutions and (ii) ensuring that the internal walls of the PDMS modules are hydrophilic.

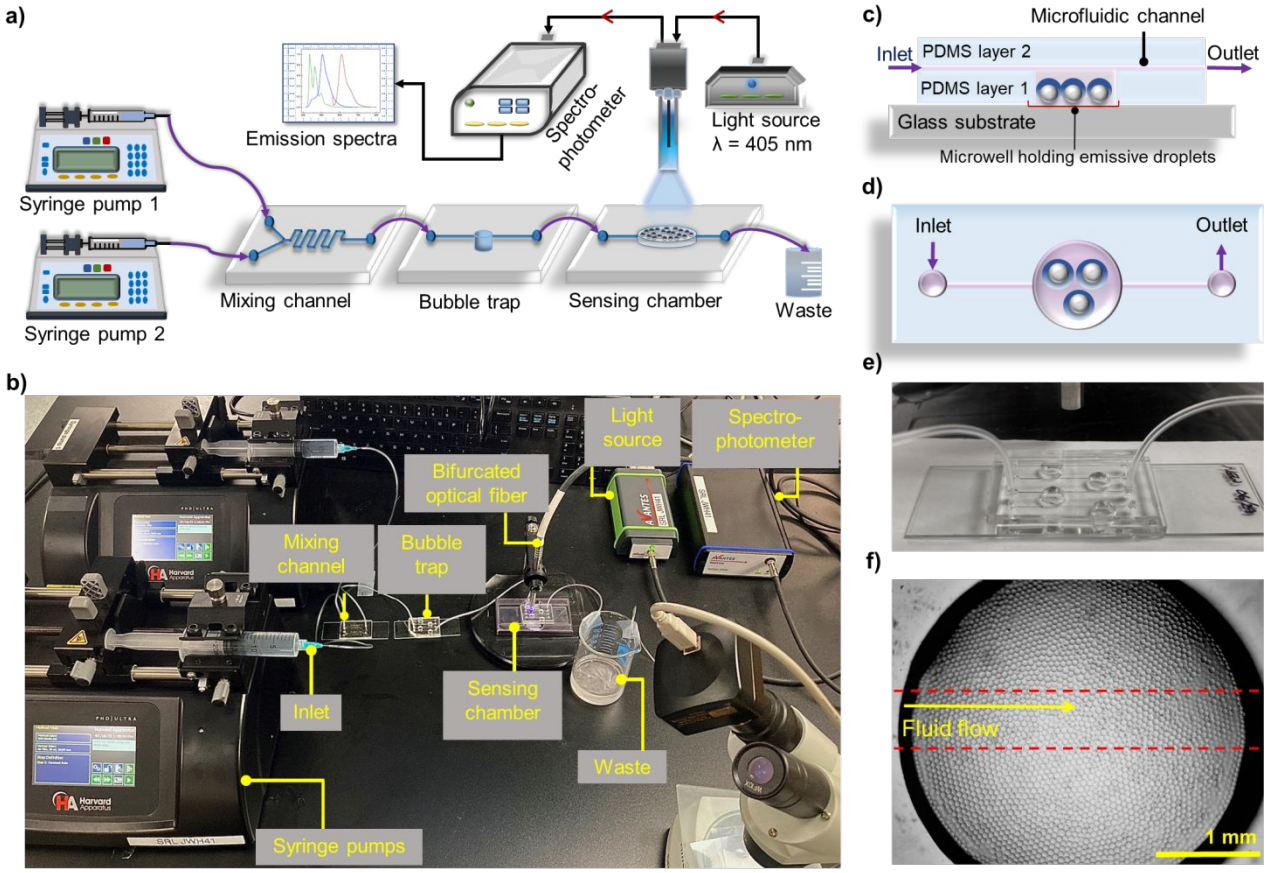

Figure 3. (a) Schematic diagram and (b) photograph of the experimental setup of PDMS microfluidics and emissive complex droplets. (c, d, e) Side-view diagram, top-view diagram, and photograph of the sensing chamber that hosts complex droplets. (f) An optical micrograph of complex droplets in a monolayer inside the sensing chamber.

Next, the complex droplets inside the sensing chamber were excited by UV light via the optical fiber placed directly above the sensing chamber. We collected emission spectra (from 340 nm to 850 nm) with the time interval of 40 millisecond and normalized the intensity of the targeted emission peaks. Additionally, we adjusted the geometry of the PDMS microchannels and the operational flow rate to improve two key metrics of performance: the physical stability of the droplets inside the sensing chamber and the response time required to achieve stabilized optical signal (**Supporting Information, Figures S6**). While higher flow rates decrease the response time, such conditions increase mechanical agitation, reduce the stability of the droplets, and decrease the reproducibility of the optical signals. For our proof-of-concept system, constant total flow rate of 200 μL min^{-1} produced sufficiently fast response time (< 2 minutes) with minimal disruption to the complex droplet monolayer.

Measurement of continuous data. To validate our sensing platform, we began with the continuous monitoring of the droplet optical properties. Specifically, we controlled the balance between γ_H and γ_F in the sensing chamber by continuously adjusting the flow rates of the two surfactant solutions (*i.e.*, f_{SDS}) and measured the emission intensity as a function of time. **Figure 4a** represents schematic diagrams of the expected droplet morphologies and emission intensity as functions of γ_H and γ_F.[11] Briefly, when complex droplets assume double emulsion (F/H/W) and Janus morphology, the fluorescent emission is dispersed. Conversely, the emission is focused upward with droplets in an inverted morphology (H/F/W), leading to a sharp increase in emission intensity. Because the transformation between each morphology is gradual and dynamic,[5] we hypothesized that such a transformation would produce a gradual and continuous measurement of the changes in fluorescent intensity.

To test this hypothesis, we measured the emission intensity at 475 nm of complex droplets with perylene dye from pure SDS solution ($f_{SDS} = 1$) to pure Capstone solution ($f_{SDS} = 0$). In pure SDS solution ($\gamma_H < \gamma_F$), complex droplets are assumed to be the F/H/W morphology and produced the lowest emission intensity, which was consistent with previous reports.[11,20,39] This minimum value served as the baseline for normalization of our data. **Figures 4b-e**

demonstrate the collected continuous emission for different flow patterns, which simulated different rates of change in interfacial tension and morphology.

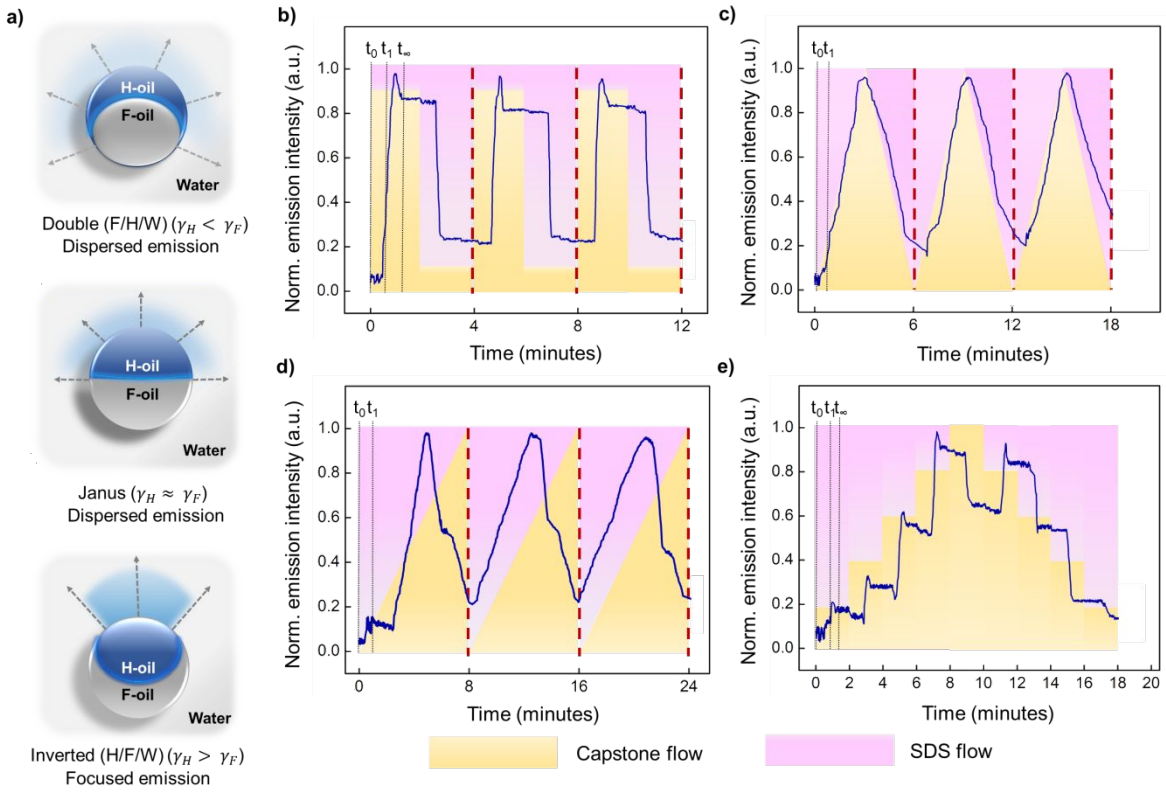

Figure 4. (a) Schematic diagrams of the three main morphologies and expected emission intensities of complex droplets. The emission intensity is a direct function of the droplet morphology and the contact angle at the triple-phase contact line (the phase boundary among H-oil, F-oil, and water). (b-e) Real-time responses to different rates of change in the ratio of SDS and Capstone (f_{SDS}) with constant total flowrate. Yellow areas represent Capstone and pink areas represent SDS.

First, we alternated between a flow of mostly SDS to a flow of mostly Capstone in a square wave pattern (**Figure 4b**). Specifically, we maintained a constant total flow rate of 200 μL min^{-1} and adjusted the ratio of flow rates from syringe pump 1 (pure Capstone, yellow area) and syringe pump 2 (pure SDS, pink area) to alternate between f_{SDS} = 0.95 and 0.05, simulating an abrupt change in γ_H and γ_F. The sharp drop in f_{SDS}, due to addition of Capstone solution transformed the emulsions from F/H/W to H/F/W, produced a significant increase in emission intensity. Prior to the equilibrium intensity, we observed a peak at the beginning of each cycle. These peaks are seen because the maximum emission intensity takes place when f_{SDS} = 0.2, as measured previously by Zeininger et al.[11] and reproduced in **Figure 2c**. However, this peak was absent when we switched back from f_{SDS} of 0.05 to 0.95 by increasing SDS concentration. We attributed this loss of finer features in the time series data to the fact that SDS is a weaker surfactant than Capstone, leading to a more gradual morphological transition.[6] While these dynamic behaviors remained consistent over multiple cycles (**Supporting Information**, **Figure S7**), slight decrease in the overall emission intensity over long experimental time occurred due to minor loss of complex droplets through bursting and coalescence.[72] Additionally, we observed consistent time delays between the input (change in f_{SDS}) and the equilibrium emission intensity. This behavior is attributed to the contributions of two lag times. First, the time delay (t_1) of 25 ± 3 seconds corresponding to the travel time from the syringe pumps to the sensing chamber. Second, the signal stabilization time (between t_1 and t_∞) was 15 ± 3 seconds, which is consistent with the time to exchange the liquid inside the sensing chamber with an approximate volume of 55 μL. **Figure 5** depicts the effects of this gradual exchange of solution inside the sensing chamber on the morphologies of the droplets. Specifically, the incoming liquid enters through the straight channel to the center of the cylindrical sensing chamber and gradually diffuses through the entire vessel, leading to the transformation of droplets in the center prior to the ones on the edge of the vessel.

Next, we measured the responses to different flow patterns to simulate different rates of change in

f_{SDS}. **Figure 4c** represents the responses to a combination of gradual ramp up and down, while **Figure 4d** shows a combination of a linear ramp up and an abrupt drop. Similar to the square-wave pattern, we observed a travel time delay (t_1) of 26 ± 2 seconds. However, there was no clear stabilization time in the signals for the linear ramp up or ramp down. We attributed this result to the slower rate of change in f_{SDS}, which matched the rate of morphological transformation of the emissive droplets. In the case of a linear ramp and an abrupt drop, we observed a manifestation of the stabilization time that appeared as a "shoulder" after the peak intensity was reached. While these deviations arose from the non-instantaneous transformation of emissive droplets, they were repeatable over multiple cycles and could potentially be alleviated by optimization of the analyte flow rates. Lastly, we measured the response to a staircase flow pattern with a change of 0.20 in f_{SDS} every two minutes (**Figure 4e**). We observed similar emission intensity changes at different f_{SDS} and demonstrated the ability to replicate, in real-time, the calibration curve constructed from the discrete experiment (**Figure 2c**). We note here that the optical signal for $f_{SDS} \sim 0$ decreased as the H-oil is fully encapsulated by the F-oil and a smaller amount of light was able leak out across the thin interface at the top of the droplet.

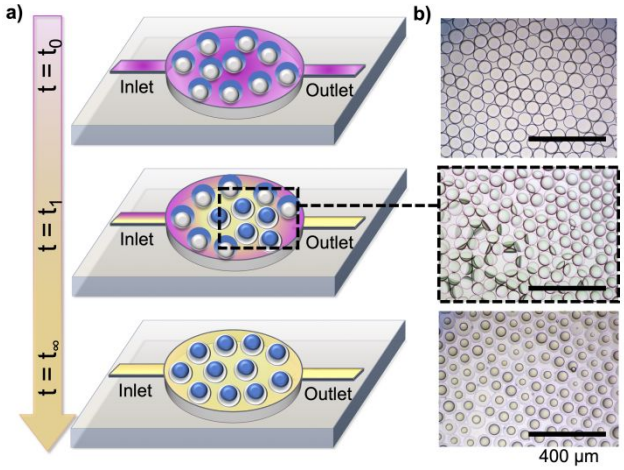

Figure 5. (a) Schematic diagrams and (b) optical micrographs of morphological transformation inside the sensing chamber. Time delay (t_1) accounts for the travel time from the syringe pumps to the sensing chamber and a stabilization time (t_∞) accounts for the transformation of droplets inside the chamber.

Generation of multiplexed signals. After we evaluated the responses from a single type of droplets to the change in surfactant composition, we sought to prove the concept of multiplexing by simultaneously measuring the fluorescent emissions generated from three types of droplets, each with a different functionalization (**Figures 6a-b**). We hypothesized that each type would act independently and provide unique emission signals. The first droplet formulation comprised single-phase droplets of ODCB with dissolved coumarin 545T fluorescent dye ("green," emission peak at λ = 505 nm). These single-phase droplets are not responsive to the changes in the surfactant solution (*i.e.*, interfacial tensions); thus, they produced consistent emission intensity and served as a control. Second, we used the same double emulsions with perylene dye ("blue," emission peak at λ = 475 nm) that are responsive to changes in γ_H and γ_F, as described in the previous section. The third group comprised pH responsive double emulsions with a fluorescent dye, lumogen red F300 ("red," emission peak at λ = 610 nm). We dissolved an amphiphilic block copolymer—polystyrene-*block*-polyacrylic acid (PS-*b*-PAA)—in the H-oil domain to serve as a co-surfactant. The block copolymer is an effective surfactant at basic pH and less effective at neutral and acidic pH.[58]

Figure 6c demonstrates the effect of changes in pH and surfactant composition on the "red" droplets with PS-*b*-PAA. The hydrophilic PAA portion is sensitive to pH changes and undergoes a reversible conformational transformation. At high values of pH, the PAA portion forms an extended coil and PS-*b*-PAA acts as a strong H-surfactant that outcompetes Capstone ($\gamma_H < \gamma_F$).[73] Thus, in a Capstone solution at pH of 12, these droplets are in double emulsions (F/H/W with low emission intensity), rather than the inverted morphology (H/F/W with high emission intensity). As we decrease the pH of the Capstone solution, PS-*b*-PAA becomes a less effective surfactant because of the globule structure of PAA and Capstone dominates ($\gamma_H > \gamma_F$), transforming the droplets into the expected inverted morphology (H/F/W) and increasing emission intensity. We note here that at low pH, these droplets behaved similarly to those without PS-*b*-PAA. The fluorescent emission intensities of this experiment are shown in **Supporting Information, Figure S8.**

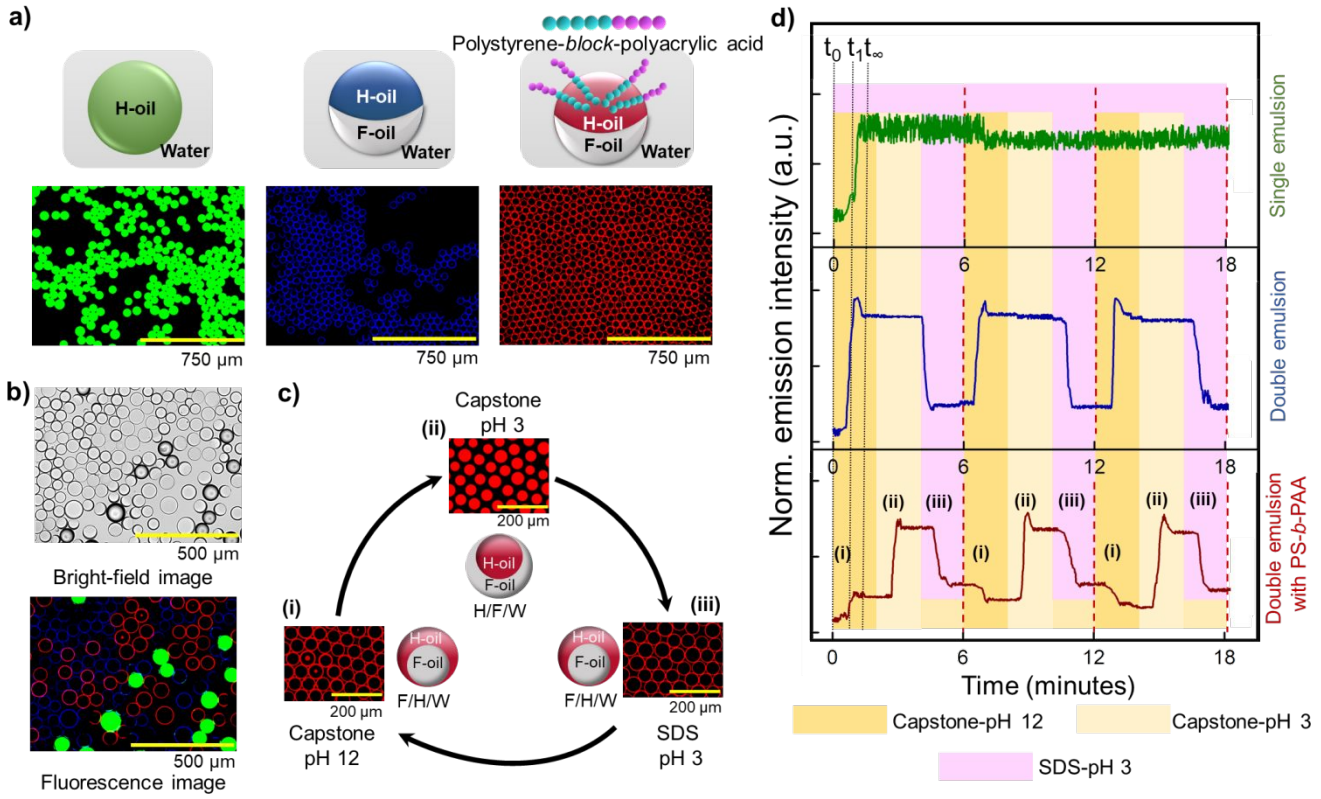

Figure 6. (a) Schematic diagrams and fluorescent micrographs of the three types of emissive droplets: single-phase droplets of ODCB with coumarin 545T dye ("green"); double emulsions with perylene dye ("blue"); and double emulsions with lumogen Red F300 dye ("red") and pH-responsive block copolymer (PS-b-PAA) as a co-surfactant. (b) Optical and fluorescent micrographs of an array with three droplet types in a shared aqueous solution. (c) Expected behavior of "red" droplets in response to changes in pH and composition of surfactants. (d) Emission intensities measured at the three characteristic wavelengths. The three regimes are (i) f_{SDS} = 0.05 at pH 12 (dark yellow), (ii) f_{SDS} = 0.05 at pH 3 (light yellow), and (iii) f_{SDS} = 0.95 at pH 3 (pink).

For the demonstration of multiplexing capability, the array of all three types of droplets was exposed together to the square-wave flow pattern that varied both the pH and surfactant compositions. **Figure 6d** depicts the emission intensities over time in three distinct regimes: **(i)** f_{SDS} = 0.05 at pH 12, dark yellow; **(ii)** f_{SDS} = 0.05 at pH 3, light yellow; and **(iii)** f_{SDS} = 0.95 at pH 3, pink. Each regime was maintained for two minutes to reach equilibrium signals. The "green" control droplets behaved as expected with no significant variation in emission intensity in the three regimes, because they only have one interface (H-oil/water) and both SDS and Capstone sufficiently reduced γ_H and stabilized the emulsion. The "blue" droplets exhibited similar behavior as shown in the previous experiments, where their morphologies were altered only due to changes in f_{SDS} and not from the changes in pH. Lastly, the "red" droplets exhibited a clear increase in the emission intensity from regime **(i)** to **(ii)** when the pH was reduced. Interestingly, we observed a slight difference in emission intensity between regime **(i)** and **(iii)**, even though most "red" droplets should assume the same double morphology (F/H/W) in these two regimes. We suspect that there are slight deviations in the values of γ_H and γ_F that led to the different emission intensity. These behaviors were consistent over consecutive cycles with the expected time delay, which validated the performance of the combination of multiple types of droplets as a multiplexed array.

As a proof-of-concept, we chose to work with two common surfactants to demonstrate the change in interfacial behaviors during continuous measurement. Moreover, for the investigation of multiplexing capability of the microfluidic sensing device, we used an amphiphilic block copolymer reported previously to imbue droplet interfaces with selectivity.[73] Potential issues regarding selectivity and interfering components in aqueous complex matrices can be solved by the addition of droplets with different functionalization to individually detect the effects of each analyte. This approach has been demonstrated previously for the selective detection of targeted analytes.[11,12,15,17–20,38,39] Furthermore, another limitation may arise from the nonmonotonic behavior of directional emission. As shown in **Figure 2c** and **Figure S4** (**Supporting Information**), the emission intensity reaches a maximum value at $f_{SDS} = 0.2$, which agrees well with previous reports that measured directional emission in a batch-to-batch manner.[11,20,39] This behavior limits the effective range of complex droplets to be from $f_{SDS} =$ 0.2 to 1. In this work, we sought to demonstrate the ability to faithfully reproduce the full range of responses from complex droplets, including the nonmonotonic response, in real-time via continuous and multiplexed measurement.

CONCLUSIONS

In conclusion, we demonstrated the combination of emissive complex droplets and PDMS microfluidic devices as a potential sensing platform for rapid diagnostic and real-time monitoring of aqueous solutions. We leveraged the dynamic and reversible optical properties of complex droplets in conjunction with PDMS devices to realize continuous monitoring. Furthermore, to prove the concept of multiplexing capability, we measured the change in emission intensity of different types of droplets with distinct characteristic emission wavelength and interfacial functionality. We showed three types of droplets with differential behaviors while exposed to the same analyte solution. On-going projects in our group are focusing on engineering interfacial functionality to selectively target relevant analytes (*e.g.*, heavy metals and PFAS). However, this report provides a simple, robust, and modular platform with potential applications in environmental monitoring and medical diagnostics.

Declaration of Competing Interest

The authors declare no conflict of interest

Acknowledgements

The research reported here was funded by the Army Research Office via grant # W911-NF-2110310 to the University of Arizona. Any opinions or errors are not those of the Army Research Office or Department of Defense and are attributable solely to the authors. This work was also supported by startup funds from the University of Arizona through the Department of Chemical and Environmental Engineering, the BIO5 Institute, and Research, Innovation, and Impact (RII). This work was performed in part at the Micro/Nano Fabrication Center at the University of Arizona.

Supplementary Materials

Supplementary materials associated with this article can be found in the online version at DOI:

References

(1) Zhang, J.; Grzybowski, B. A.; Granick, S. Janus Particle Synthesis, Assembly, and Application. *Langmuir* **2017**, acs.langmuir.7b01123. https://doi.org/10.1021/acs.langmuir.7b01123.

(2) Forth, J.; Kim, P. Y.; Xie, G.; Liu, X.; Helms, B. A.; Russell, T. P. Building Reconfigurable Devices Using Complex Liquid–Fluid Interfaces. *Adv.*

Mater. **2019**, *31* (18), 1–39. https://doi.org/10.1002/adma.201806370.

(3) McClements, D. J.; Li, Y. Structured Emulsion-Based Delivery Systems: Controlling the Digestion and Release of Lipophilic Food Components. *Adv. Colloid Interface Sci.* **2010**, *159* (2), 213–228. https://doi.org/10.1016/j.cis.2010.06.010.

(4) Yazan, Y.; Seiller, M.; Puisieux, F. *Multiple Emulsions*; 1993; Vol. 132. https://doi.org/10.1515/9783110541953-006.

(5) Zarzar, L. D.; Sresht, V.; Sletten, E. M.; Kalow, J. A.; Blankschtein, D.; Swager, T. M. Dynamically Reconfigurable Complex Emulsions via Tunable Interfacial Tensions. *Nature* **2015**, *518* (7540), 520–524. https://doi.org/10.1038/nature14168.

(6) Balaj, R. V; Zarzar, L. D. Reconfigurable Complex Emulsions: Design, Properties, and Applications. *Chem. Phys. Rev.* **2020**, *1* (1), 011301. https://doi.org/10.1063/5.0028606.

(7) Lin, C.-J.; Zeininger, L.; Savagatrup, S.; Swager, T. M. Morphology-Dependent Luminescence in Complex Liquid Colloids. *J. Am. Chem. Soc.* **2019**, *141* (9), 3802–3806. https://doi.org/10.1021/jacs.8b13215.

(8) Jia, K.; Zhang, X.; Zhang, L.; Yu, L.; Wu, Y.; Li, L.; Mai, Y.; Liao, B. Photoinduced Reconfiguration of Complex Emulsions Using a Photoresponsive Surfactant. *Langmuir* **2018**, *34* (38), 11544–11552. https://doi.org/10.1021/acs.langmuir.8b02456.

(9) Wang, X.; Zhou, Y.; Palacio-Betancur, V.; Kim, Y. K.; Delalande, L.; Tsuei, M.; Yang, Y.; De Pablo, J. J.; Abbott, N. L. Reconfigurable Multicompartment Emulsion Drops Formed by Nematic Liquid Crystals and Immiscible Perfluorocarbon Oils. *Langmuir* **2019**, *35* (49), 16312–16323. https://doi.org/10.1021/acs.langmuir.9b02864.

(10) Nagelberg, S.; Zarzar, L. D.; Subramanian, K.; Sresht, V.; Blankschtein, D.; Barbastathis, G.; Kreysing, M.; Swager, T. M.; Kolle, M. Reconfigurable and Dynamically Tunable Droplet-Based Compound Micro-Lenses. *Opt. InfoBase Conf. Pap.* **2018**, *Part F95-3* (2015), 14673. https://doi.org/10.1364/3D.2018.3W3G.2.

(11) Zeininger, L.; Nagelberg, S.; Harvey, K. S.; Savagatrup, S.; Herbert, M. B.; Yoshinaga, K.; Capobianco, J. A.; Kolle, M.; Swager, T. M. Rapid Detection of Salmonella Enterica via Directional Emission from Carbohydrate-Functionalized Dynamic Double Emulsions. *ACS Cent. Sci.* **2019**, *5* (5), 789. https://doi.org/10.1021/acscentsci.9b00059.

(12) Zhang, Q.; Savagatrup, S.; Kaplonek, P.; Seeberger, P. H.; Swager, T. M. Janus Emulsions for the Detection of Bacteria. *ACS Cent. Sci.* **2017**, *3* (4), 309–313. https://doi.org/10.1021/acscentsci.7b00021.

(13) Kang, D.-K.; Ali, M. M.; Zhang, K.; Huang, S. S.; Peterson, E.; Digman, M. a; Gratton, E.; Zhao, W. Rapid Detection of Single Bacteria in Unprocessed Blood Using Integrated Comprehensive Droplet Digital Detection. *Nat. Commun.* **2014**, *5* (1), 5427. https://doi.org/10.1038/ncomms6427.

(14) Zhao, X.; Cui, Y.; Wang, J.; Wang, J. Preparation of Fluorescent Molecularly Imprinted Polymers via Pickering Emulsion Interfaces and the Application for Visual Sensing Analysis of Listeria Monocytogenes. *Polymers*. 2019. https://doi.org/10.3390/polym11060984.

(15) Li, J.; Savagatrup, S.; Nelson, Z.; Yoshinaga, K.; Swager, T. M. Fluorescent Janus Emulsions for Biosensing of Listeria Monocytogenes. *Proc. Natl. Acad. Sci.* **2020**, *117* (22), 11923–11930. https://doi.org/10.1073/pnas.2002623117.

(16) Day, A. S.; Ulep, T. H.; Safavinia, B.; Hertenstein, T.; Budiman, E.; Dieckhaus, L.; Yoon, J. Y. Emulsion-Based Isothermal Nucleic Acid Amplification for Rapid SARS-CoV-2 Detection via Angle-Dependent Light Scatter Analysis. *Biosens. Bioelectron.* **2021**, *179* (December 2020), 113099. https://doi.org/10.1016/j.bios.2021.113099.

(17) Li, J.; Concellón, A.; Yoshinaga, K.; Nelson, Z.; He, Q.; Swager, T. M. Janus Emulsion Biosensors for Anti-SARS-CoV-2 Spike Antibody. *ACS Cent. Sci.* **2021**, *7* (7), 1166–1175. https://doi.org/10.1021/acscentsci.1c00173.

(18) Wang, M. S.; Nitin, N. Rapid Detection of Bacteriophages in Starter Culture Using Water-in-Oil-in-Water Emulsion Microdroplets. *Appl. Microbiol. Biotechnol.* **2014**, *98* (19), 8347–8355. https://doi.org/10.1007/s00253-014-6018-7.

(19) Pavlovic, M.; Ramiya Ramesh Babu, H. K.; Djalali, S.; Vraneš, M.; Radonić, V.; Zeininger, L. Facile Monitoring of Water Hardness Levels Using Responsive Complex Emulsions. *Anal. Chem.* **2021**, *93* (27), 9390–9396. https://doi.org/10.1021/acs.analchem.1c00868.

(20) Trinh, V.; Malloy, C. S.; Durkin, T. J.; Gadh, A.; Savagatrup, S. Detection of PFAS and Fluorinated Surfactants Using Differential Behaviors at Interfaces of Complex Droplets. *ACS Sensors* **2022**, *7* (5), 1514–1523. https://doi.org/10.1021/acssensors.2c00257.

(21) Kumar, V.; Kukkar, D.; Hashemi, B.; Kim, K.-H.; Deep, A. Advanced Functional Structure-Based Sensing and Imaging Strategies for Cancer.Pdf. *Adv. Funct. Mater.* **2019**, *29* (16).

(22) Jain, R.; Thakur, A.; Kaur, P.; Kim, K. H.; Devi, P. Advances in Imaging-Assisted Sensing Techniques for Heavy Metals in Water: Trends, Challenges, and Opportunities. *TrAC - Trends Anal. Chem.* **2020**, *123*, 115758. https://doi.org/10.1016/j.trac.2019.115758.

(23) Huang, L.; Tian, S.; Zhao, W.; Liu, K.; Ma, X.; Guo, J. Multiplexed Detection of Biomarkers in Lateral-Flow Immunoassays. *Analyst* **2020**, *145* (8), 2828–2840. https://doi.org/10.1039/c9an02485a.

(24) Channon, R. B.; Yang, Y.; Feibelman, K. M.; Geiss, B. J.; Dandy, D. S.; Henry, C. S. Development of an

Electrochemical Paper-Based Analytical Device for Trace Detection of Virus Particles. *Anal. Chem.* **2018**, *90* (12), 7777–7783. https://doi.org/10.1021/acs.analchem.8b02042.

(25) Dincer, C.; Bruch, R.; Kling, A.; Dittrich, P. S.; Urban, G. A. Multiplexed Point-of-Care Testing – XPOCT. *Trends Biotechnol.* **2017**, *35* (8), 728–742. https://doi.org/10.1016/j.tibtech.2017.03.013.

(26) Zhou, J.; Mukherjee, P.; Gao, H.; Luan, Q.; Papautsky, I. Label-Free Microfluidic Sorting of Microparticles. *APL Bioeng.* **2019**, *3* (4), 041504. https://doi.org/10.1063/1.5120501.

(27) Han, X.; Liu, Y.; Yin, J.; Yue, M.; Mu, Y. Microfluidic Devices for Multiplexed Detection of Foodborne Pathogens. *Food Res. Int.* **2021**, *143* (November 2020), 110246. https://doi.org/10.1016/j.foodres.2021.110246.

(28) Jayamohan, H.; Lambert, C. J.; Sant, H. J.; Jafek, A.; Patel, D.; Feng, H.; Beeman, M.; Mahmood, T.; Nze, U.; Gale, B. K. SARS-CoV-2 Pandemic: A Review of Molecular Diagnostic Tools Including Sample Collection and Commercial Response with Associated Advantages and Limitations. *Anal. Bioanal. Chem.* **2021**, *413* (1), 49–71. https://doi.org/10.1007/s00216-020-02958-1.

(29) Zamora-Ledezma, C.; Negrete-Bolagay, D.; Figueroa, F.; Zamora-Ledezma, E.; Ni, M.; Alexis, F.; Guerrero, V. H. Heavy Metal Water Pollution: A Fresh Look about Hazards, Novel and Conventional Remediation Methods. *Environ. Technol. Innov.* **2021**, *22*, 101504. https://doi.org/10.1016/j.eti.2021.101504.

(30) Nayak, S.; Blumenfeld, N. R.; Laksanasopin, T.; Sia, S. K. Point-of-Care Diagnostics: Recent Developments in a Connected Age. *Anal. Chem.* **2017**, *89* (1), 102–123. https://doi.org/10.1021/acs.analchem.6b04630.

(31) Jung, W.; Han, J.; Choi, J. W.; Ahn, C. H. Point-of-Care Testing (POCT) Diagnostic Systems Using Microfluidic Lab-on-a-Chip Technologies. *Microelectron. Eng.* **2015**, *132*, 46–57. https://doi.org/10.1016/j.mee.2014.09.024.

(32) Rebe Raz, S.; Haasnoot, W. Multiplex Bioanalytical Methods for Food and Environmental Monitoring. *TrAC - Trends Anal. Chem.* **2011**, *30* (9), 1526–1537. https://doi.org/10.1016/j.trac.2011.04.016.

(33) Bake, K. D.; Walt, D. R. Multiplexed Spectroscopic Detections. *Annu. Rev. Anal. Chem.* **2008**, *1* (1), 515–547. https://doi.org/10.1146/annurev.anchem.1.031207.112826.

(34) Wilson, G. S.; Gifford, R. Biosensors for Real-Time in Vivo Measurements. *Biosens. Bioelectron.* **2005**, *20* (12), 2388–2403. https://doi.org/10.1016/j.bios.2004.12.003.

(35) Cass, A. E. G.; Sharma, S. *Microneedle Enzyme Sensor Arrays for Continuous In Vivo Monitoring*, 1st ed.; Elsevier Inc., 2017; Vol. 589. https://doi.org/10.1016/bs.mie.2017.02.002.

(36) Tric, M.; Lederle, M.; Neuner, L.; Dolgowjasow, I.; Wiedemann, P.; Wölfl, S.; Werner, T. Optical Biosensor Optimized for Continuous In-Line Glucose Monitoring in Animal Cell Culture. *Anal. Bioanal. Chem.* **2017**, *409* (24), 5711–5721. https://doi.org/10.1007/s00216-017-0511-7.

(37) Deiss, D.; Szadkowska, A.; Gordon, D.; Mallipedhi, A.; Schütz-Fuhrmann, I.; Aguilera, E.; Ringsell, C.; De Block, C.; Irace, C. Clinical Practice Recommendations on the Routine Use of Eversense, the First Long-Term Implantable Continuous Glucose Monitoring System. *Diabetes Technol. Ther.* **2019**, *21* (5), 254–264. https://doi.org/10.1089/dia.2018.0397.

(38) Zarzar, L. D.; Kalow, J. A.; He, X.; Walish, J. J.; Swager, T. M. Optical Visualization and Quantification of Enzyme Activity Using Dynamic Droplet Lenses. *Proc. Natl. Acad. Sci.* **2017**, *114* (15), 3821–3825. https://doi.org/10.1073/pnas.1618807114.

(39) Fong, D.; Swager, T. M. Trace Detection of Hydrogen Peroxide via Dynamic Double Emulsions. *J. Am. Chem. Soc.* **2021**, *143* (11), 4397–4404. https://doi.org/10.1021/jacs.1c00683.

(40) Ku, K. H.; McDonald, B. R.; Vijayamohanan, H.; Zentner, C. A.; Nagelberg, S.; Kolle, M.; Swager, T. M. Dynamic Coloration of Complex Emulsions by Localization of Gold Rings Near the Triphase Junction. *Small* **2021**, *17* (12), 2007507. https://doi.org/10.1002/smll.202007507.

(41) Roy, P.; Liu, S.; Dutcher, C. S. Droplet Interfacial Tensions and Phase Transitions Measured in Microfluidic Channels. *Annu. Rev. Phys. Chem.* **2020**, *72*, 73–97. https://doi.org/10.1146/annurev-physchem-090419-105522.

(42) Steegmans, M. L. J.; Warmerdam, A.; Schroen, K. G. P. H.; Boom, R. M. Dynamic Interfacial Tension Measurements with Microfluidic Y-Junctions. *Langmuir* **2009**, *25* (17), 9751–9758. https://doi.org/10.1021/la901103r.

(43) Dhar, B. C.; Lee, N. Y. Lab-on-a-Chip Technology for Environmental Monitoring of Microorganisms. *Biochip J.* **2018**, *12* (3), 173–183. https://doi.org/10.1007/s13206-018-2301-5.

(44) Pol, R.; Céspedes, F.; Gabriel, D.; Baeza, M. Microfluidic Lab-on-a-Chip Platforms for Environmental Monitoring. *TrAC - Trends Anal. Chem.* **2017**, *95*, 62–68. https://doi.org/10.1016/j.trac.2017.08.001.

(45) Li, S.; Zhang, C.; Wang, S.; Liu, Q.; Feng, H.; Ma, X.; Guo, J. Electrochemical Microfluidics Techniques for Heavy Metal Ion Detection. *Analyst* **2018**, *143* (18), 4230–4246. https://doi.org/10.1039/c8an01067f.

(46) Hudson, S. D.; Cabral, J. T.; Goodrum, W. J.; Beers, K. L.; Amis, E. J. Microfluidic Interfacial Tensiometry. *Appl. Phys. Lett.* **2005**, *87* (8), 2003–2006. https://doi.org/10.1063/1.2034098.

(47) Cabral, J. T.; Hudson, S. D. Microfluidic Approach

for Rapid Multicomponent Interfacial Tensiometry. *Lab Chip* **2006**, *6* (3), 427–436. https://doi.org/10.1039/b511976f.

(48) Gu, H.; Duits, M. H. G.; Mugele, F. Interfacial Tension Measurements with Microfluidic Tapered Channels. *Colloids Surfaces A Physicochem. Eng. Asp.* **2011**, *389* (1–3), 38–42. https://doi.org/10.1016/j.colsurfa.2011.08.054.

(49) Martin, J. D.; Hudson, S. D. Mass Transfer and Interfacial Properties in Two-Phase Microchannel Flows. *New J. Phys.* **2009**, *11*. https://doi.org/10.1088/1367-2630/11/11/115005.

(50) D'Apolito, R.; Perazzo, A.; D'Antuono, M.; Preziosi, V.; Tomaiuolo, G.; Miller, R.; Guido, S. Measuring Interfacial Tension of Emulsions in Situ by Microfluidics. *Langmuir* **2018**, *34* (17), 4991–4997. https://doi.org/10.1021/acs.langmuir.8b00208.

(51) Lee, D.; Fang, C.; Ravan, A. S.; Fuller, G. G.; Shen, A. Q. Temperature Controlled Tensiometry Using Droplet Microfluidics. *Lab Chip* **2017**, *17* (4), 717–726. https://doi.org/10.1039/c6lc01384h.

(52) Wang, X.; Riaud, A.; Wang, K.; Luo, G. Pressure Drop-Based Determination of Dynamic Interfacial Tension of Droplet Generation Process in T-Junction Microchannel. *Microfluid. Nanofluidics* **2015**, *18* (3), 503–512. https://doi.org/10.1007/s10404-014-1449-0.

(53) Brosseau, Q.; Vrignon, J.; Baret, J. C. Microfluidic Dynamic Interfacial Tensiometry (MDIT). *Soft Matter* **2014**, *10* (17), 3066–3076. https://doi.org/10.1039/c3sm52543k.

(54) Wang, K.; Lu, Y. C.; Xu, J. H.; Luo, G. S. Determination of Dynamic Interfacial Tension and Its Effect on Droplet Formation in the T-Shaped Microdispersion Process. *Langmuir* **2009**, *25* (4), 2153–2158. https://doi.org/10.1021/la803049s.

(55) Li, S.; Xu, J.; Wang, Y.; Luo, G. A New Interfacial Tension Measurement Method through a Pore Array Micro-Structured Device. *J. Colloid Interface Sci.* **2009**, *331* (1), 127–131. https://doi.org/10.1016/j.jcis.2008.11.017.

(56) Simón Marqués, P.; Frank, B. D.; Savateev, A.; Zeininger, L. Janus Emulsion Solar Concentrators as Photocatalytic Droplet Microreactors. *Adv. Opt. Mater.* **2021**, *9* (24), 2101139. https://doi.org/10.1002/adom.202101139.

(57) Savagatrup, S.; Ma, D.; Zhong, H.; Harvey, K. S.; Kimerling, L. C.; Agarwal, A. M.; Swager, T. M. Dynamic Complex Emulsions as Amplifiers for On-Chip Photonic Cavity-Enhanced Resonators. *ACS Sensors* **2020**, *5* (7), 1996–2002. https://doi.org/10.1021/acssensors.0c00399.

(58) Chen, Q.; Vancso, G. J. PH Dependent Elasticity of Polystyrene-Block-Poly(Acrylic Acid) Vesicle Shell Membranes by Atomic Force Microscopy. *Macromolecular Rapid Communications*. 2011, pp 1704–1709. https://doi.org/10.1002/marc.201100332.

(59) Jang, J. H.; Park, S. Y. PH-Responsive Cholesteric Liquid Crystal Double Emulsion Droplets Prepared by Microfluidics. *Sensors Actuators, B Chem.* **2017**, *241*, 636–643. https://doi.org/10.1016/j.snb.2016.10.118.

(60) Sparks, D. J.; Romero-González, M. E.; El-Taboni, E.; Freeman, C. L.; Hall, S. A.; Kakonyi, G.; Swanson, L.; Banwart, S. A.; Harding, J. H. Adsorption of Poly Acrylic Acid onto the Surface of Calcite: An Experimental and Simulation Study. *Phys. Chem. Chem. Phys.* **2015**, *17* (41), 27357–27365. https://doi.org/10.1039/c5cp00945f.

(61) Friend, J.; Yeo, L. Fabrication of Microfluidic Devices Using Polydimethylsiloxane. *Biomicrofluidics* **2010**, *4* (2). https://doi.org/10.1063/1.3259624.

(62) Raj M, K.; Chakraborty, S. PDMS Microfluidics: A Mini Review. *J. Appl. Polym. Sci.* **2020**, *137* (27), 1–14. https://doi.org/10.1002/app.48958.

(63) Shakeri, A.; Khan, S.; Didar, T. F. Conventional and Emerging Strategies for the Fabrication and Functionalization of PDMS-Based Microfluidic Devices. *Lab Chip* **2021**, *21* (16), 3053–3075. https://doi.org/10.1039/d1lc00288k.

(64) Kim, P.; Kwon, K. W.; Park, M. C.; Lee, S. H.; Kim, S. M.; Suh, K. Y. Soft Lithography for Microfluidics: A Review. *Biochip J.* **2008**, *2* (1), 1–11.

(65) Lake, J. R.; Heyde, K. C.; Ruder, W. C. Low-Cost Feedback-Controlled Syringe Pressure Pumps for Microfluidics Applications. *PLoS ONE*. 2017. https://doi.org/10.1371/journal.pone.0175089.

(66) Lee, C. Y.; Chang, C. L.; Wang, Y. N.; Fu, L. M. Microfluidic Mixing: A Review. *Int. J. Mol. Sci.* **2011**, *12* (5), 3263–3287. https://doi.org/10.3390/ijms12053263.

(67) Bragheri, F.; Vázquez, R. M.; Osellame, R. *Microfluidics*; 2019. https://doi.org/10.1016/B978-0-12-817827-0.00057-6.

(68) Gao, Y.; Wu, M.; Lin, Y.; Xu, J. Trapping and Control of Bubbles in Various Microfluidic Applications. *Lab Chip* **2020**, *20* (24), 4512–4527. https://doi.org/10.1039/d0lc00906g.

(69) Hoek, I.; Tho, F.; Arnold, W. M. Sodium Hydroxide Treatment of PDMS Based Microfluidic Devices. *Lab Chip* **2010**, *10* (17), 2283–2285. https://doi.org/10.1039/c004769d.

(70) Lee, J. N.; Park, C.; Whitesides, G. M. Solvent Compatibility of Poly(Dimethylsiloxane)-Based Microfluidic Devices. *Anal. Chem.* **2003**, *75* (23), 6544–6554. https://doi.org/10.1021/ac0346712.

(71) Vinothkumar, T. S.; Kandaswamy, D.; Arathi, G.; Dinesh, K. Influence of Different Organic Solvents on Degree of Swelling of Poly (Dimethyl Siloxane)-Based Sealer. *J. Conserv. Dent.* **2011**, *14* (2), 156–159. https://doi.org/10.4103/0972-0707.82621.

(72) Ho, T. M.; Razzaghi, A.; Ramachandran, A.; Mikkonen, K. S. Emulsion Characterization via Microfluidic Devices: A Review on Interfacial

Tension and Stability to Coalescence. *Adv. Colloid Interface Sci.* **2022**, *299* (October 2021), 102541. https://doi.org/10.1016/j.cis.2021.102541.

(73) Durkin, T. J.; Barua, B.; Savagatrup, S. Modification of Amphiphilic Block Copolymers for Responsive and Biologically Active Surfactants in Complex Droplets. *Giant* **2023**, *13*, 100134. https://doi.org/10.1016/j.giant.2022.100134.